
Efficient Transfer Learning in Diffusion Models via Adversarial Noise

Xiyu Wang¹, Baijiong Lin², Daochang Liu¹, Chang Xu¹

¹ School of Computer Science, Faculty of Engineering, The University of Sydney

² The Hong Kong University of Science and Technology (Guangzhou)

{xiyuwang.usyd, bj.lin.email}@gmail.com

{daochang.liu, c.xu}@sydney.edu.au

Abstract

Diffusion Probabilistic Models (DPMs) have demonstrated substantial promise in image generation tasks but heavily rely on the availability of large amounts of training data. Previous works, like GANs, have tackled the limited data problem by transferring pre-trained models learned with sufficient data. However, those methods are hard to be utilized in DPMs since the distinct differences between DPM-based and GAN-based methods, showing in the unique iterative denoising process integral and the need for many timesteps with no-targeted noise in DPMs. In this paper, we propose a novel DPMs-based transfer learning method, TAN, to address the limited data problem. It includes two strategies: similarity-guided training, which boosts transfer with a classifier, and adversarial noise selection which adaptive chooses targeted noise based on the input image. Extensive experiments in the context of few-shot image generation tasks demonstrate that our method is not only efficient but also excels in terms of image quality and diversity when compared to existing GAN-based and DDPM-based methods.

1 Introduction

Generative models, such as GANs [7, 1, 13], VAEs [14, 22], and autoregressive models [28, 4, 8], have made remarkable successes in various fields across images [1, 21], text [2], and audio [6, 20] by utilizing vast amounts of unlabeled data for training. Diffusion probabilistic models (DPMs) [25, 9, 17], which are designed to replicate data distributions by learning to invert multi-step noise procedures, have recently experienced significant advancements, enabling the generation of high-definition images with broad diversity. Although DPMs have emerged as a potent tool for image generation with remarkable results in terms of both quality and diversity, modern DPMs heavily rely on extensive amounts of data to train the large-scale parameters of their networks [3]. This dependency can lead to overfitting and a failure to generate diverse, high-quality images with limited training data. Unfortunately, gathering sufficient data is not always feasible in certain situations.

Transfer learning can be an effective solution to this challenge, as it applies knowledge from a pre-trained generative model trained on a large dataset to a smaller one. The fundamental idea is to begin training with a source model that has been pre-trained on a large dataset, and then adapt it to a target domain with limited data. Several techniques have been proposed in the past to adapt pre-trained GAN-based models [29, 11, 30, 15] from large-scale source datasets to target datasets using a limited number of training samples. Typically, methods for few-shot image generation either enhance the training data artificially using data augmentation to prevent overfitting [32, 11], or directly evaluate the distance between the processed image and the target image [19, 33].

Nevertheless, applying prior GAN-based techniques to DPMs is challenging due to the differences in training processes between GAN-based and DPM-based methods. GANs can quickly generate a

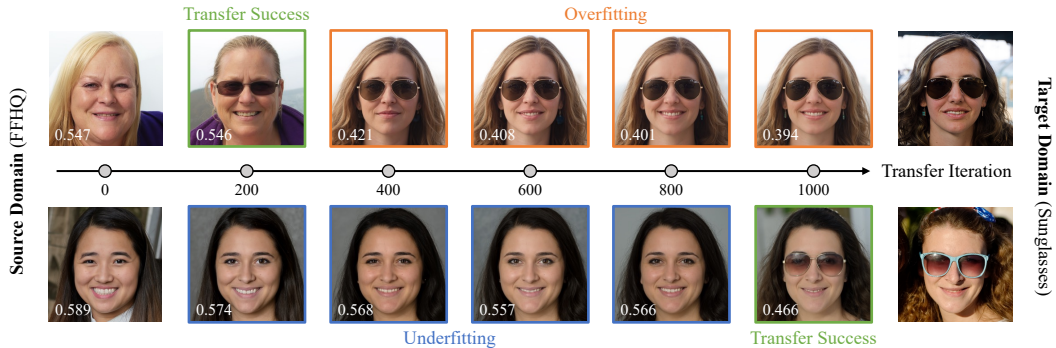


Figure 1: Two sets of images generated from corresponding fixed noise inputs at different stages of fine-tuning DDPM from FFHQ to 10-shot Sunglasses. The perceptual distance (LPIPS [32]) with the training target image is shown on each generated image. When the bottom image successfully transfers to the target domain, the top image has already suffered from overfitting.

final processed image from latent space, while DPMs only predict less noisy images at each step and request large timesteps to generate a high-quality final image. Such an iterative denoising process poses two challenges when transferring diffusion models. The first challenge is that the transfer direction needs to be estimated on noisy images. The single-pass generation of GANs allows them to directly compare the generated clean images with the target image [15, 19, 33], which is not easily applicable to diffusion models. The current DPM-based few-shot method, DDPM pairwise adaptation (DDPM-PA) [34], substitutes the high-quality real final image with the predicted blurry final at the intermediate timestep to address this issue. However, comparing the target image with the blurry image can be problematic and inaccurate, as the predicted image may not accurately represent the domain of generated images. It leads to the production of DDPM-PA final images that are fuzzy and distorted. Moreover, even if the transfer direction can be available, we still face a more fundamental second challenge resulting from the noise mechanism in diffusion models. The diffusion and denoising process utilize fully random Gaussian noise, which is independent of the input image and makes no assumption of it. We observe that such non-targeted noise imposes unbalanced effects on different images, leading to divergent transferring pace in terms of training iteration needed. As demonstrated in Figure 1, when one image (below) is just successfully transferred from the source domain to the target domain, another image (above) may have severely overfit and become too similar to the target image. Such normally distributed noise may also necessitate an extensive number of iterations to transfer, especially when the gradient direction is noisy due to limited images.

In this paper, to handle the challenge of transferring direction estimation for diffusion models, we propose to leverage a similarity measurement to estimate the gap between the source and the target, which circumvents the necessity of comparing individual images. Building upon this, we introduce a *similarity-guided training* approach to fine-tune the pre-trained source model to the target domain. It employs a classifier to estimate the divergence between the source and target domains, leveraging existing knowledge from the source domain to aid in training the target domain. This method not only helps in bridging the gap between the source and target domains for diffusion models but also addresses the unstable gradient direction caused by limited target data in the few-shot setting by implicitly comparing the sparse target data with the abundant source data. More importantly, to tackle the challenge of non-targeted noise in diffusion models, we propose a novel min-max training process, i.e., *adversarial noise selection*, to dynamically choose the noise according to the input image. The adversarial noise scheme enhances few-shot transfer learning by minimizing the “worse-case” Gaussian noise which the pre-trained model fails to denoise on the target dataset. This strategy also significantly reduces the training iterations needed and largely improves the efficiency of the transfer learning for diffusion models. Our adversarial strategy with similarity measurement excels in few-shot image generation tasks, speeding up training, achieving quicker convergence, and creating images fitting the target style while resembling source images. Our Experiments on few-shot image generation tasks demonstrate our method surpasses existing GAN-based and DDPM-based techniques, offering superior quality and diversity.

2 Related Work

2.1 Diffusion Probabilistic Models

Ho et al. [9] has been leveraged as an effective generative model that circumvents the adversarial training inherent in GANs [7]. DDPMs, by enabling the diffusion reverse process, are capable of reconstructing images. However, due to their extensive iterative time steps, DDPMs are subject to the challenge of high computational time. DDIM [26] addresses this issue by "implicating" the model, which allows it to function with far fewer iterations and dramatically reduces the inference time compared to DDPM. Conversely, a fresh approach to the diffusion model is the score-based model via SDE, wherein the diffusion and the denoising processes are both modeled by SDEs. Song and Ermon [27] initially proposed the generation of samples from latent noise via the Dynamic Langevin Sampling method. For fast high-quality, high-resolution image generation, Latent Diffusion Models (LDMs) [23] propose an advanced machine learning methodology by gradually transforming a random noise into the target image through a diffusion process that uses latent space representations.

2.2 Few-shot Image Generation

Existing practices predominantly adopt an adaptation pipeline where a foundational model is pre-trained on a large source domain, and then adjusted to a smaller target domain. In contrast, few-shot image generation strives to envision new and diverse examples while circumventing overfitting to the limited training images. CDC [19] introduces a cross-domain consistency loss and patch-level discrimination to forge a connection between the source and target domains. DCL [33] uses contrastive learning to distance the generated samples from actual images and maximize the similarity between corresponding image pairs in source and target domains. The DDPM-PA [34] adopts a similar approach to CDC for adapting models pre-trained on extensive source domains to target domains. GAN-based methods, like CDC and DCL, require the final generated image during training. In contrast, DPMs' training process aims to predict the next stage of noised images and can only yield a blurry predicted image during the training stage.

3 Preliminary

Gaussian diffusion models are used to approximate the data distribution $x_0 \sim q(x_0)$ by $p_\theta(x_0)$. The distribution $p_\theta(x_0)$ is modeled in the form of latent variable models. According to [9], the diffusion process from a data distribution to a Gaussian distribution with variance $\beta_t \in (0, 1)$ for timestep t can be expressed as:

$$q(x_t|x_0) = \mathcal{N}(x_t; \bar{\alpha}_t x_0, (1 - \bar{\alpha}_t)\mathbf{I}),$$

$$x_t = \sqrt{\bar{\alpha}_t}x_0 + \sqrt{1 - \bar{\alpha}_t}\epsilon,$$

where $\alpha_t := 1 - \beta_t$, $\bar{\alpha}_t := \prod_{i=0}^t (1 - \beta_i)$ and $\epsilon \sim \mathcal{N}(\mathbf{0}, \mathbf{I})$. Ho et al. [9] trains a U-Net [24] model parameterized by θ to fit the data distribution $q(x_0)$ by maximizing the variational lower-bound. The DDPM training loss with model $\epsilon_\theta(x_t, t)$ can be expressed as:

$$\mathcal{L}_{\text{sample}}(\theta) := \mathbb{E}_{t, x_0, \epsilon} \|\epsilon - \epsilon_\theta(x_t, t)\|^2. \quad (1)$$

Based on [26], the reverse process of DDPM and DDIM at timestep t can be expressed as:

$$x_{t-1} = \underbrace{\sqrt{\bar{\alpha}_{t-1}} \left(\frac{x_t - \sqrt{1 - \bar{\alpha}_t} \epsilon_\theta(x_t, t)}{\bar{\alpha}_t} \right)}_{\text{predicted } x_0} + \underbrace{\sqrt{1 - \bar{\alpha}_{t-1} - \sigma_t^2} \cdot \epsilon_\theta(x_t, t)}_{\text{direction pointing to } x_t} + \underbrace{\sigma_t \epsilon_t}_{\text{random noise}},$$

where $\sigma_t = \eta \sqrt{(1 - \bar{\alpha}_{t-1}) / (1 - \bar{\alpha}_t)} \sqrt{1 - \bar{\alpha}_t / \bar{\alpha}_{t-1}}$ and $\eta = 0$ [26] or $\eta = 1$ [9] or $\eta = \sqrt{(1 - \bar{\alpha}_t) / (1 - \bar{\alpha}_{t-1})}$ [9]. Enhance, Dhariwal and Nichol [5] propose the conditional reverse noise process as:

$$p_{\theta, \phi}(x_{t-1}|x_t, y) \approx \mathcal{N}(x_{t-1}; \mu_\theta(x_t, t) + \sigma_t^2 \gamma \nabla_{x_t} \log p_\phi(y|x_t), \sigma_t^2 \mathbf{I}), \quad (2)$$

$$\text{where } \mu_\theta(x_t, t) = \frac{1}{\sqrt{\alpha_t}} \left(x_t - \frac{1 - \alpha_t}{\sqrt{1 - \bar{\alpha}_t}} \epsilon_\theta(x_t, t) \right), \quad (3)$$

and γ is a hyperparameter for conditional control. For the sake of clarity in distinguishing domains, this paper uses \mathcal{S} and \mathcal{T} to represent the source and target domain, respectively.

4 Method

4.1 Transfer Learning in Diffusion Models via Adversarial Noise

In this subsection, we introduce transfer learning in diffusion models via Adversarial Noise, TAN, with similarity-guided training and adversarial noise selection for stronger transfer ability. Given the challenges associated with generating the final image, we suggest using similarity to measure the gap between the source and target domains using a noised image x_t at timestep t . Drawing inspiration from [5, 16], we express the domain difference between the source and target in terms of the divergence in similarity measures.

Initially, we assume a model that can predict noise with both source and target domains, denoted as $\theta_{(\mathcal{S}, \mathcal{T})}$. As Equation (2), the reverse process for the source and target images can be written as:

$$p_{\theta_{(\mathcal{S}, \mathcal{T})}, \phi}(x_{t-1}|x_t, y = Y) \approx \mathcal{N}(x_{t-1}; \mu_{\theta_{(\mathcal{S}, \mathcal{T})}} + \sigma_t^2 \gamma \nabla_{x_t} \log p_{\phi}(y = Y|x_t), \sigma_t^2 \mathbf{I}), \quad (4)$$

where Y is \mathcal{S} or \mathcal{T} for source or target domain image generation, respectively. We can consider $\mu(x_t) + \sigma_t^2 \gamma \nabla_{x_t} \log p_{\phi}(y = \mathcal{S}|x_t)$ as the source model $\theta_{\mathcal{S}}$, which only synthesizes image on the source domain respectively. For brevity, we denote $p_{\theta_{\mathcal{S}}, \phi}(x_{t-1}^{\mathcal{S}}|x_t) = p_{\theta_{(\mathcal{S}, \mathcal{T})}, \phi}(x_{t-1}|x_t, y = \mathcal{S})$. We similarly define $p_{\theta_{\mathcal{T}}, \phi}(x_{t-1}^{\mathcal{T}}|x_t)$ as above by replacing \mathcal{S} with \mathcal{T} . Therefore, the KL-divergence between the output of source model $\theta_{\mathcal{S}}$ and the target $\theta_{\mathcal{T}}$ with the same input x_t at timestep t , is defined as follows:

$$\begin{aligned} & \text{D}_{\text{KL}}(p_{\theta_{\mathcal{S}}, \phi}(x_{t-1}^{\mathcal{S}}|x_t), p_{\theta_{\mathcal{T}}, \phi}(x_{t-1}^{\mathcal{T}}|x_t)) \\ &= \mathbb{E}_{t, x_0, \epsilon} \left[\left\| \nabla_{x_t} \log p_{\phi}(y = \mathcal{S}|x_t) - \nabla_{x_t} \log p_{\phi}(y = \mathcal{T}|x_t) \right\|^2 \right], \end{aligned} \quad (5)$$

where p_{ϕ} is a classifier to distinguish x_t . The detailed derivation is in Appendix. We consider the $\nabla_{x_t} \log p_{\phi}(y = \mathcal{S}|x_t)$ and $\nabla_{x_t} \log p_{\phi}(y = \mathcal{T}|x_t)$ as the similarity measures of the given x_t in the source and target domains, respectively. Since x_t pertains to the target image during fine-tuning, the term $p_{\phi}(y = \mathcal{S}|x_t^{\mathcal{T}})$ is near zero and its gradient is large and chaotic. Therefore, we disregard the first term and utilize only $p_{\phi}(y = \mathcal{T}|x_t^{\mathcal{T}})$ to guide the training process. Specifically, we employ a fixed pre-trained binary classifier that differentiates between source and target images at time step t to boost the training process. Similarly with the vanilla training loss in DPMs [9], i.e., Equation (1), we use the KL-divergence between the output of current model θ and target model $\theta_{\mathcal{T}}$ at time step t as:

$$\min_{\theta} \mathbb{E}_{t, x_0, \epsilon} \left[\left\| \epsilon_t - \epsilon_{\theta}(x_t, t) - \hat{\sigma}_t^2 \gamma \nabla_{x_t} \log p_{\phi}(y = \mathcal{T}|x_t) \right\|^2 \right], \quad (6)$$

where $\epsilon_t \sim \mathcal{N}(\mathbf{0}, \mathbf{I})$, ϵ_{θ} is the pre-trained neural network on source domain, γ is a hyper-parameter to control the similarity guidance, $\hat{\sigma}_t = (1 - \bar{\alpha}_{t-1}) \sqrt{\frac{\alpha_t}{1 - \bar{\alpha}_t}}$, and p_{ϕ} is the binary classifier differentiating between source and target images. Equation (6) is defined as similarity-guided DPMs train loss. The full proof is provided in the Appendix. We leverage the pre-trained classifier to indirectly compare the noised image x_t with both domain images, subtly expressing the gap between the currently generated image and the target image. By minimizing the output of the neural network with corrected noise, we bridge the gap in the diffusion model and bolster transfer learning. Furthermore, similarity guidance enhances few-shot transfer learning by avoiding misdirection towards the target image, as $\nabla_{x_t} \log p_{\phi}(y = \mathcal{T}|x_t)$ acts as an indirect indicator, rather than straightly relying on the original image.

Despite potentially determining the transfer direction, we still encounter a fundamental second challenge originating from the noise mechanism in diffusion models. As mentioned, the model needs to be trained to accommodate the quantity of noise ϵ_t over many iterations. However, increasing iterations with limited images may lead to overfitting of the training samples, thereby reducing the diversity of the generated samples. On the other hand, training with too few iterations might only successfully transform a fraction of the generated images into the target domain as Figure 1.

To counter these issues, we propose an adaptive noise selection method. This approach utilizes a min-max training process to reduce the actual training iterations required and ensure the generated images closely resemble the target images. After the model has been trained on a large dataset, it exhibits a strong noise reduction capability for source datasets. This implies it only needs to minimize specific types of Gaussian noise with which the trained model struggles or fails to denoise with the

target domain sample. The first step in this process is to identify the maximum Gaussian noise with the current model, and then specifically minimize the model using this noise. Based on Equation (6), this can be mathematically formulated as follows:

$$\min_{\theta} \max_{\epsilon} \mathbb{E}_{t, x_0} \left[\left\| \epsilon - \epsilon_{\theta}(x_t, t) - \sigma_t^2 \gamma \nabla_{x_t} \log p_{\phi}(y = \mathcal{T}|x_t) \right\|^2 \right]. \quad (7)$$

Although finding the exact maximum noise is challenging as Equation (7), the projected gradient descent (PGD) strategy can be used to solve the inner maximization problem instead. Specifically, the inner maximization of Gaussian noise can be interpreted as finding the “worse-case” noise corresponding to the current neural network. Practically, the similarity-guided term is disregarded, as this term is hard to compute differential and is almost unchanged in the process. We utilize the multi-step variant of PGD with gradient ascent, as expressed below:

$$\epsilon^{j+1} = \text{Norm} \left(\epsilon^j + \omega \nabla_{\epsilon^j} \left\| \epsilon^j - \epsilon_{\theta}(\sqrt{\alpha_t} x_0 + \sqrt{1 - \alpha_t} \epsilon^j, t) \right\|^2 \right), \quad j = 0, \dots, J - 1, \quad (8)$$

where ω is a hyperparameter that represents the “learning rate” of the negative loss function, and Norm is a normalization function that approximately ensures the mean and standard deviation of ϵ^{j+1} is $\mathbf{0}$ and \mathbf{I} respectively. The initial value, ϵ_0 , is sampled from the Gaussian distribution as $\epsilon_0 \sim \mathcal{N}(\mathbf{0}, \mathbf{I})$. We use this method to identify this worse-case noise and minimizing the “worse-case” Gaussian noise is akin to minimizing all Gaussian noises that are “better” than it. By adaptively choosing this specific noise, we can more accurately correct the gradient to enhance training with limited data, effectively addressing the underfitting problem during a limited number of iterations.

4.2 Optimization

For time and GPU memory saving, we implement an additional adaptor module, ψ^l , [18] to learn the shift gap as Equation (5) based on x_t in practice. During the training, we keep the parameters of θ^l constant and update the additional adaptor layer parameters ψ^l . The overall loss function can be expressed as follows,

$$L(\psi) \equiv \mathbb{E}_{t, x_0} \left\| \epsilon^* - \epsilon_{\theta, \psi}(x_t^*, t) - \sigma_t^2 \gamma \nabla_{x_t^*} \log p_{\phi}(y = \mathcal{T}|x_t^*) \right\|^2 \quad (9)$$

$$\text{s.t. } \epsilon^* = \arg \max_{\epsilon} \left\| \epsilon - \epsilon_{\theta}(\sqrt{\alpha_t} x_0 + \sqrt{1 - \alpha_t} \epsilon, t) \right\|^2, \quad \epsilon_{\text{mean}}^* = \mathbf{0} \text{ and } \epsilon_{\text{std}}^* = \mathbf{I}, \quad (10)$$

where ϵ^* is the “worse-case” noise, the $x_t^* = \sqrt{\alpha_t} x_0 + \sqrt{1 - \alpha_t} \epsilon^*$ is the corresponding noised image at the timestep t and ψ is certain extra parameter beyond pre-trained model. We link the pre-trained U-Net model with the adaptor layer [10] as $x_t^l = \theta^l(x_t^{l-1}) + \psi^l(x_t^{l-1})$, where x_t^{l-1} and x_t^l represents the l -th layer of the input and output, and θ^l and ψ^l denote the l -th layer of the pre-trained U-Net and the additional adaptor layer, respectively.

Algorithm 1 Training DPMs with TAN

Require: binary classifier p_{ϕ} , pre-trained DPMs ϵ_{θ} , learning rate η

- 1: **repeat**
 - 2: $x_0 \sim q(x_0)$;
 - 3: $t \sim \text{Uniform}(\{1, \dots, T\})$;
 - 4: $\epsilon \sim \mathcal{N}(\mathbf{0}, \mathbf{I})$;
 - 5: **for** $j = 0, \dots, J - 1$ **do**
 - 6: Update ϵ^j via Eq. (8);
 - 7: **end for**
 - 8: Compute $L(\psi)$ with $\epsilon^* = \epsilon^J$ via Eq. (9);
 - 9: Update the adaptor model parameter: $\psi = \psi - \eta \nabla_{\psi} L(\psi)$;
 - 10: **until** converged.
-

The full training procedure of our method, named DPMs-TAN, is outlined in Algorithm 1. Initially, as in the traditional DDPM training process, we select samples from target datasets and randomly choose a timestep t and standard Gaussian noise for each sample. we employ limited extra adaptor module parameters with the pre-train model. Subsequently, we identify the adaptive inner max as represented in Equation (8) with the current neural network. Based on these noises, we compute the similarity-guided DDPM loss as Equation (6), which bridges the discrepancy between the pre-trained model and the scarce training samples. Lastly, we execute backpropagation to only update the adaptor module parameters.

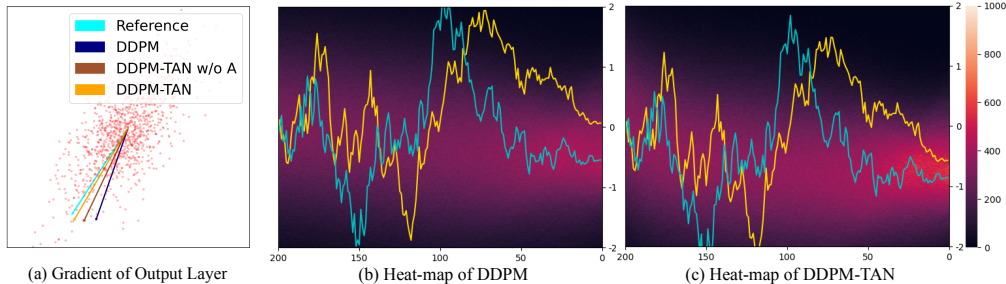


Figure 2: This Figure visualizes gradient changes and heat maps: Figure (a) shows gradient directions with various settings—the cyan line for the gradient of 10,000 samples in one step, dark blue for ten samples in one step as baseline method (trained with traditional DDPM), the sienna for our similarity-guided training, and the orange for our method DDPM-TAN, while red points at the background are "worse"-case noises by adversarial noise selection; Figure (b) and (c) depict heat-maps of the baseline and our method, with cyan and gold lines representing the generation sampling process value with the original DDPM and our method, respectively.

5 Experiment

To demonstrate the effectiveness of our approach, we perform a series of few-shot image generation experiments using a limited set of just 10 training images with the same setting as DDPM-PA [34]. We compare our method against state-of-the-art GAN-based and DDPM-based techniques, assessing the quality and diversity of the generated images through both qualitative and quantitative evaluations. This comprehensive comparison provided strong evidence of the superiority of our proposed method in the context of few-shot image generation tasks.

5.1 Visualization on Toy Data

To conduct a quantitative analysis, we trained a diffusion model to generate 2-dimensional toy data with two Gaussian noise distributions. The means of the Gaussian noise distributions for the source and target are $(1, 1)$ and $(-1, -1)$, and their variances are denoted by \mathbf{I} . We train a simple neural network with source domain samples and then transfer this pre-trained model to target samples.

Figure 2 (a) illustrates the output layer gradient direction of four different settings in the first iteration, with the same noise and timestep t . The red line, computed with ten thousand different samples, is considered a reliable reference direction (close to 45 degrees southwest). For 10-shot samples, we repeat them a thousand times into one batch to provide a unified comparison with ten thousand different samples. The dark blue line and the sienna represent the gradient computed with the traditional DDPM as the baseline and similarity-guided training in a 10-shot sample, respectively. The orange line represents our method, DDPM-TAN, in a 10-shot sample. The gradient of our method is closer to the reliable reference direction, demonstrating that our approach can effectively correct the issue of the noisy gradient. The red points in the background symbolize "worse-case" noise, which is generated through adversarial noise selection. The graphic shows how the noise distribution transitions from a circle (representing a normal Gaussian distribution) to an ellipse. The principal axis of this ellipse is oriented along the gradient of the model parameters. This illustrates the noise distribution shift under our adversarial noise selection approach, which effectively fine-tunes the model by actively targeting the "worst-case" noise that intensifies the adaptation task.

Figures 2 (b) and (c) present heatmaps of the baseline and our method in only one dimension, respectively. The cyan and gold lines denote the values of the generation sampling process using the original DDPM and our method. The heat-maps in the background illustrate the distribution of values for 20,000 samples generated by the original DDPM (baseline) and our method. The lighter the color in the background, the greater the number of samples present. There is a significantly brighter central highlight in (c) compared to (b), demonstrating that our method can learn the distribution more quickly than the baseline method. The gold and cyan lines in the two figures are approximately parallel, providing further evidence that our method can learn the gap, as per Equation (5), more rapidly.



Figure 3: The 10-shot image generation samples on LSUN Church \rightarrow Landscape drawings (top) and FFHQ \rightarrow Raphael’s paintings (bottom). When compared with other GAN-based and DDPM-based methods, our method, TAN, yields high-quality results that more closely resemble images of the target domain style, with less blurring.

5.2 Experimental Setup

Datasets. Following [19], we use FFHQ [12] and LSUN Church [31] as source datasets. For the target datasets, we employ 10-shot Sketches, Babies, Sunglasses, and face paintings by Amedeo Modigliani and Raphael Peale, which correspond to the source domain FFHQ. Additionally, we utilize 10-shot Haunted Houses and Landscape drawings as target datasets corresponding to the LSUN Church source domain.

Configurations. We evaluate our method not only on the DDPM framework but also on the LDMs. For this, we employ a pre-trained DDPM similar to DDPM-PA and use the pre-trained LDMs as provided in [23]. We restrict our fine-tuning to the shift module of the U-Net, maintaining the pre-trained DPMs and autoencoders in LDMs as they are. For the l -th shift adaptor layer ψ , it can be expressed as: $\psi^l(x^{l-1}) = f(x^{l-1}W_{down})W_{up}$ [10]. We project the input downward using W_{down} , transforming it from its original dimension $\mathbb{R}^{w \times h \times r}$ to a lower-dimensional space with a bottleneck dimension $\mathbb{R}^{\frac{w}{c} \times \frac{h}{c} \times d}$. Following this, we apply a non-linear activation function $f(\cdot)$ and execute an upward projection with W_{up} . For the DDPMs, we set the parameters $c = 4$ and $d = 8$, whereas we set $c = 2$ and $d = 8$ for the LDMs. To ensure the adapter layer outputs are initialized to zero, we set all the extra layer parameters to zero. For similarity-guided training, we establish $\gamma = 5$. In the case of adversarial noise selection, we assign $J = 10$ and $\omega = 0.02$ for most transfer learning tasks. We employ a learning rate of 5×10^{-5} for the DDPMs or 1×10^{-5} LDMs for approximately 300 iterations with a batch size of 40 on $\times 8$ NVIDIA A100.

Measurements. In our evaluation of generation diversity, we utilize Intra-LPIPS and FID as described in CDC [19]. For Intra-LPIPS, we generate 1,000 images, which each of them will be assigned to the training sample with the smallest LPIPS distance. The Intra-LPIPS measurement is obtained by averaging the pairwise LPIPS distances within the same cluster and then averaging these results across all clusters. FID is a widely use metric for assessing the generation quality of generative

Table 1: The Intra-LPIPS (\uparrow) results for both DDPM-based strategies and GAN-based baselines are presented for 10-shot image generation tasks. These tasks involve adapting from the source domains of FFHQ and LSUN Church. The ‘‘Parameter Rate’’ column provides information regarding the proportion of parameters fine-tuned in comparison to the pre-trained model’s parameters. The best results are marked as **bold**.

Methods	Parameter Rate	FFHQ \rightarrow Babies	FFHQ \rightarrow Sunglasses	FFHQ \rightarrow Raphael’s paintings	LSUN Church \rightarrow Haunted houses	LSUN Church \rightarrow Landscape drawings
TGAN	100%	0.510 \pm 0.026	0.550 \pm 0.021	0.533 \pm 0.023	0.585 \pm 0.007	0.601 \pm 0.030
TGAN+ADA	100%	0.546 \pm 0.033	0.571 \pm 0.034	0.546 \pm 0.037	0.615 \pm 0.018	0.643 \pm 0.060
EWC	100%	0.560 \pm 0.019	0.550 \pm 0.014	0.541 \pm 0.023	0.579 \pm 0.035	0.596 \pm 0.052
CDC	100%	0.583 \pm 0.014	0.581 \pm 0.011	0.564 \pm 0.010	0.620 \pm 0.029	0.674 \pm 0.024
DCL	100%	0.579 \pm 0.018	0.574 \pm 0.007	0.558 \pm 0.033	0.616 \pm 0.043	0.626 \pm 0.021
DDPM-PA	100%	0.599 \pm 0.024	0.604 \pm 0.014	0.581 \pm 0.041	0.628 \pm 0.029	0.706 \pm 0.030
DDPM-TAN (Ours)	1.3%	0.592 \pm 0.016	0.613 \pm 0.023	0.621 \pm 0.068	0.648 \pm 0.010	0.723 \pm 0.020
LMD-TAN (Ours)	1.6%	0.601 \pm 0.018	0.613 \pm 0.011	0.592 \pm 0.048	0.653 \pm 0.010	0.738 \pm 0.026

models by calculating the distribution distances between generated samples and datasets. However, FID may become unstable and unreliable when applied to datasets with few samples, such as the 10-shot datasets used in this paper. Following the DDPM-PA approach, we provide FID evaluations using larger target datasets, such as Sunglasses and Babies, which consist of 2,500 and 2,700 images, respectively.

Baselines. To adapt pre-trained models to target domains using a limited number of samples, we compare our work with several GAN-based and DDPMs baselines that share similar objectives. These include TGAN [29], TGAN+ADA [11], EWC [15], CDC [19], DCL [33], and DDPM-PA [34]. All these methods are implemented on the same StyleGAN2 [12] codebase.

5.3 Overall Performance

Qualitative Evaluation. Figure 3 presents samples from GAN-based and DDPM-based methods for 10-shot LSUN Church \rightarrow Landscape drawings (top) and FFHQ \rightarrow Raphael’s paintings (bottom). The samples generated by GAN-based baselines contain unnatural blurs and artifacts. This illustrates the effectiveness of our approach in handling complex transformations while maintaining the integrity of the original image features. Whereas the current DDPM-based method, DDPM-PA (third row), seems to underfit the target domain images, resulting in a significant difference in color and style between the generated images and the target images.

Our method preserves many source domain shapes and outlines while learning more about the target style. As demonstrated in Figure 1, our method, TAN, maintains more details such as buildings (above) and human faces (below) in the generated images. Moreover, TAN-generated images exhibit a color style closer to the target domain, especially when compared with DDPM-PA. Compared to other methods, our approach (based on both DDPMs and LDMs) produces more diverse and realistic samples that contain richer details than existing techniques.

Table 2: FID (\downarrow) results of each method on 10-shot FFHQ \rightarrow Babies and Sunglasses. The best results are marked as **bold**.

Methods	TGAN	ADA	EWC	CDC	DCL	PA	ADMT
Babies	104.79	102.58	87.41	74.39	52.56	48.92	46.70
Sunglasses	55.61	53.64	59.73	42.13	38.01	34.75	20.06

Quantitative Evaluation. In Table 1, we display the Intra-LPIPS results for DPMS-TAN under various 10-shot adaptation conditions. DDPM-TAN yields a considerable improvement in Intra-LPIPS across most tasks when compared with other GAN-based and DDPMs-based methods. Furthermore, LMD-TAN excels beyond state-of-the-art GAN-based approaches, demonstrating its potent capability to preserve diversity in few-shot image generation. The FID results are presented in Table 2, where TAN also demonstrates remarkable advancements compared to other GAN-based or DPMS-based methods, especially in FFHQ \rightarrow 10-shot Sunglasses with 20.06 FID. We provide more results for other adaptation scenarios in the Appendix.

Our method can transfer the model from the source to the target domain not only effectively but also efficiently. Compared to other methods that require around 5,000 iterations, our approach only necessitates approximately 300 iterations with limited parameter fine-tuning. We use the direct fine-tuning on DDPM as our baseline, utilizing a batch size of 5 on one GPU. The time cost of the baseline



Figure 4: This figure shows our ablation study with all models trained for 300 iterations on a 10-shot sunglasses dataset measured with FID (\downarrow): the first line - baseline (direct fine-tuning model), second line - Adaptor (fine-tuning only few extra parameters), third line - DPMs-TAN w/o A (only using similarity-guided training), and final line - DPMs-TAN (our method).

with 5,000 iterations (same with DDPM-PA) is 7.5 GPU hours, while our model (DPMs-TAN) with only 300 iterations takes just 3 GPU hours. Regarding GPU memory consumption, the baseline model requires 20 GB, while DPMs-TAN only uses 9 GB. Consequently, our method allows for a significant reduction in both time and GPU usage.

5.4 Ablation Analysis

Figure 4 presents an ablation study, with all images synthesized from the same noise. When compared to directly fine-tuning the entire model (1st row), only fine-tuning the adaptor layer (2nd row) can achieve competitive FID results (38.65 vs. 41.88). The DPMs-TAN without adversarial noise selection (DPMs-TAN w/o A) and all DPMs-TAN (3rd and 4th row) are trained with an extra adaptor layer to save time and GPU memory, and our analysis focuses on the last three rows.

The first two columns demonstrate that all methods can successfully transfer the model to sunglasses, with the TAN containing richer high-frequency details about sunglasses and background items. The 3rd and 4th columns show that the similarity-guided method (3rd row) can produce images of people wearing sunglasses, while the traditional method (2nd row) does not achieve this. The last two columns highlight the effectiveness of the adaptive noise selection method in TAN. The step-by-step transformation showcased in the 5th column provides a clear demonstration of how our method transfers the source face through an intermediate phase, in which the face is adorned with glasses, to a final result where the face is wearing sunglasses. This vividly illustrates the effectiveness of our proposed strategies in progressively boosting the transfer process. The Frechet Inception Distance (FID) scores further illustrate the effectiveness of our proposed strategies; it decreases from 41.88 (with direct adaptation) to 26.41 (with similarity-guided training) and then to 20.66 (with DPMs-TAN), indicating a progressive improvement in the quality of generated images.

6 Conclusion

In conclusion, the application of previous GAN-based techniques to DPMs encounters substantial challenges due to the distinct training processes of these models. To overcome this, we introduce TAN to train the DPMs with a novel adversarial noise selection and the similarity-guided strategy that improves the efficiency of the transfer learning process. Our proposed method accelerates training, achieves quicker convergence, and produces images that fit the target style while resembling the source images. Experimental results on few-shot image generation tasks demonstrate that our method surpasses existing state-of-the-art GAN-based and DDPM-based methods, delivering superior image quality and diversity.

References

- [1] A. Brock, J. Donahue, and K. Simonyan. Large scale GAN training for high fidelity natural image synthesis. *arXiv preprint arXiv:1809.11096*, 2018.
- [2] T. Brown, B. Mann, N. Ryder, M. Subbiah, J. D. Kaplan, P. Dhariwal, A. Neelakantan, P. Shyam, G. Sastry, A. Askell, et al. Language models are few-shot learners. In *Neural Information Processing Systems*, 2020.
- [3] H. Cao, C. Tan, Z. Gao, G. Chen, P.-A. Heng, and S. Z. Li. A survey on generative diffusion model. *arXiv preprint arXiv:2209.02646*, 2022.
- [4] X. Chen, N. Mishra, M. Rohaninejad, and P. Abbeel. Pixelsnail: An improved autoregressive generative model. In *International Conference on Machine Learning*, 2018.
- [5] P. Dhariwal and A. Nichol. Diffusion models beat gans on image synthesis. In *Neural Information Processing Systems*, 2021.
- [6] P. Dhariwal, H. Jun, C. Payne, J. W. Kim, A. Radford, and I. Sutskever. Jukebox: A generative model for music. *arXiv preprint arXiv:2005.00341*, 2020.
- [7] I. Goodfellow, J. Pouget-Abadie, M. Mirza, B. Xu, D. Warde-Farley, S. Ozair, A. Courville, and Y. Bengio. Generative adversarial networks. *Communications of the ACM*, 63(11):139–144, 2020.
- [8] J.-B. Grill, F. Strub, F. Altché, C. Tallec, P. Richemond, E. Buchatskaya, C. Doersch, B. Avila Pires, Z. Guo, M. Gheshlaghi Azar, et al. Bootstrap your own latent a new approach to self-supervised learning. In *Neural Information Processing Systems*, 2020.
- [9] J. Ho, A. Jain, and P. Abbeel. Denoising diffusion probabilistic models. In *Neural Information Processing Systems*, 2020.
- [10] N. Houlsby, A. Giurghi, S. Jastrzebski, B. Morrone, Q. De Laroussilhe, A. Gesmundo, M. Attariyan, and S. Gelly. Parameter-efficient transfer learning for nlp. In *International Conference on Machine Learning*, 2019.
- [11] T. Karras, M. Aittala, J. Hellsten, S. Laine, J. Lehtinen, and T. Aila. Training generative adversarial networks with limited data. In *Neural Information Processing Systems*, 2020.
- [12] T. Karras, S. Laine, M. Aittala, J. Hellsten, J. Lehtinen, and T. Aila. Analyzing and improving the image quality of stylegan. In *IEEE/CVF Conference on Computer Vision and Pattern Recognition*, 2020.
- [13] S. Khan, M. Naseer, M. Hayat, S. W. Zamir, F. S. Khan, and M. Shah. Transformers in vision: A survey. *ACM Computing Surveys*, 54(10s):1–41, 2022.
- [14] D. P. Kingma and M. Welling. Auto-encoding variational bayes. *arXiv preprint arXiv:1312.6114*, 2013.
- [15] Y. Li, R. Zhang, J. Lu, and E. Shechtman. Few-shot image generation with elastic weight consolidation. *arXiv preprint arXiv:2012.02780*, 2020.
- [16] X. Liu, D. H. Park, S. Azadi, G. Zhang, A. Chopikyan, Y. Hu, H. Shi, A. Rohrbach, and T. Darrell. More control for free! image synthesis with semantic diffusion guidance. In *IEEE/CVF Winter Conference on Applications of Computer Vision*, 2023.
- [17] A. Q. Nichol and P. Dhariwal. Improved denoising diffusion probabilistic models. In *International Conference on Machine Learning*, 2021.
- [18] A. Noguchi and T. Harada. Image generation from small datasets via batch statistics adaptation. In *IEEE/CVF International Conference on Computer Vision*, 2019.
- [19] U. Ojha, Y. Li, J. Lu, A. A. Efros, Y. J. Lee, E. Shechtman, and R. Zhang. Few-shot image generation via cross-domain correspondence. In *IEEE/CVF Conference on Computer Vision and Pattern Recognition*, 2021.
- [20] A. v. d. Oord, S. Dieleman, H. Zen, K. Simonyan, O. Vinyals, A. Graves, N. Kalchbrenner, A. Senior, and K. Kavukcuoglu. Wavenet: A generative model for raw audio. *arXiv preprint arXiv:1609.03499*, 2016.
- [21] A. Razavi, A. Van den Oord, and O. Vinyals. Generating diverse high-fidelity images with VQ-VAE-2. In *Neural Information Processing Systems*, 2019.
- [22] D. J. Rezende, S. Mohamed, and D. Wierstra. Stochastic backpropagation and approximate inference in deep generative models. In *International Conference on Machine Learning*, 2014.

- [23] R. Rombach, A. Blattmann, D. Lorenz, P. Esser, and B. Ommer. High-resolution image synthesis with latent diffusion models. In *IEEE/CVF Conference on Computer Vision and Pattern Recognition*, 2022.
- [24] O. Ronneberger, P. Fischer, and T. Brox. U-net: Convolutional networks for biomedical image segmentation. In *Medical Image Computing and Computer-Assisted Intervention*, 2015.
- [25] J. Sohl-Dickstein, E. Weiss, N. Maheswaranathan, and S. Ganguli. Deep unsupervised learning using nonequilibrium thermodynamics. In *International Conference on Machine Learning*, 2015.
- [26] J. Song, C. Meng, and S. Ermon. Denoising diffusion implicit models. *arXiv preprint arXiv:2010.02502*, 2020.
- [27] Y. Song and S. Ermon. Generative modeling by estimating gradients of the data distribution. In *Neural Information Processing Systems*, 2019.
- [28] A. Van den Oord, N. Kalchbrenner, L. Espeholt, O. Vinyals, A. Graves, et al. Conditional image generation with pixelcnn decoders. In *Neural Information Processing Systems*, 2016.
- [29] Y. Wang, C. Wu, L. Herranz, J. Van de Weijer, A. Gonzalez-Garcia, and B. Raducanu. Transferring gans: generating images from limited data. In *European Conference on Computer Vision*, 2018.
- [30] Y. Wang, A. Gonzalez-Garcia, D. Berga, L. Herranz, F. S. Khan, and J. v. d. Weijer. Minegan: effective knowledge transfer from gans to target domains with few images. In *IEEE/CVF Conference on Computer Vision and Pattern Recognition*, 2020.
- [31] F. Yu, A. Seff, Y. Zhang, S. Song, T. Funkhouser, and J. Xiao. Lsun: Construction of a large-scale image dataset using deep learning with humans in the loop. *arXiv preprint arXiv:1506.03365*, 2015.
- [32] R. Zhang, P. Isola, A. A. Efros, E. Shechtman, and O. Wang. The unreasonable effectiveness of deep features as a perceptual metric. In *IEEE Conference on Computer Vision and Pattern Recognition*, 2018.
- [33] Y. Zhao, H. Ding, H. Huang, and N.-M. Cheung. A closer look at few-shot image generation. In *IEEE/CVF Conference on Computer Vision and Pattern Recognition*, 2022.
- [34] J. Zhu, H. Ma, J. Chen, and J. Yuan. Few-shot image generation with diffusion models. *arXiv preprint arXiv:2211.03264*, 2022.

Appendix for “Efficient Transfer Learning in Diffusion Models via Adversarial Noise”

A Experiment

In this section, we present Intra-LPIPS evaluation results on two additional datasets for 10-shot transformations, FFHQ \rightarrow Sketches and FFHQ \rightarrow Amedeo’s paintings. We also provide supplementary information detailing our selection process for the hyper-parameters.

A.1 Additional Results

Quantitative Evaluation. As depicted in Table 3, our proposed DPMs-TAN method demonstrates superior performance over contemporary GAN-based and DPMs-based methods in terms of generation diversity for the given adaptation scenarios in FFHQ \rightarrow Sketches and FFHQ \rightarrow Amedeo’s paintings. Especially, we achieve 0.544 ± 0.025 for the FFHQ \rightarrow Sketches, far more better than other methods.

Qualitative Evaluation. In Figure 5, we provide additional results for GAN-based and DDPM-based methods for the 10-shot FFHQ \rightarrow Sunglasses and Babies task. When compared to the GAN-based method (shown in the 2nd and 3rd rows), our approach (shown in the 5th and 6th rows) generates images of faces wearing sunglasses, displaying a wide variety of detailed hairstyles and facial features. Moreover, DPMs-TAN produces samples with more vivid and realistic reflections in the sunglasses. Notably, our method also manages to generate more realistic backgrounds.

A.2 Hyper-parameters

In this subsection, we delve into our process for selecting key hyperparameters, including γ for the similarity-guided training, ω for the adversarial noise selection, and the count of training iterations. All experiments are conducted using a pre-trained LDM, and for evaluation purposes, we generate 1000 images for the Intra-LPIPS evaluation and 10000 images for the FID.

Table 4: This shows the change in FID (\downarrow) and Intra-LPIPS (\uparrow) results for FFHQ \rightarrow Sunglasses as the γ value increases.

γ	FID (\downarrow)	Intra-LPIPS (\uparrow)
1	20.75	0.641 ± 0.014
3	18.86	0.627 ± 0.013
5	18.13	0.613 ± 0.011
7	24.12	0.603 ± 0.017
9	29.48	0.592 ± 0.017

Similarity-guided Training Scale γ . Table 4 shows the changes in FID (\downarrow) and Intra-LPIPS (\uparrow) scores for FFHQ \rightarrow Sunglasses as the γ (in Equation (7)) increases. Initially, the FID score decrease, as the generated images gradually become closer to the target domain. At $\gamma = 5$, the FID reaches its lowest value of 18.13. Beyond this point, the FID score increases as the generated images become too similar to the target images or become random noise as failed case, leading to lower diversity and

Table 3: The Intra-LPIPS (\uparrow) results for both DDPM-based strategies and GAN-based baselines are presented for 10-shot image generation tasks. The best results are marked as **bold**.

Methods	FFHQ \rightarrow Sketches	FFHQ \rightarrow Amedeo’s paintings
TGAN	0.394 ± 0.023	0.548 ± 0.026
TGAN+ADA	0.427 ± 0.022	0.560 ± 0.019
EWC	0.430 ± 0.018	0.594 ± 0.028
CDC	0.454 ± 0.017	0.620 ± 0.029
DCL	0.461 ± 0.021	0.616 ± 0.043
DDPM-PA	0.495 ± 0.024	0.626 ± 0.022
DDPM-TAN (Ours)	0.544 ± 0.025	0.620 ± 0.021

fidelity. The Intra-LPIPS score consistently decreases with gamma increasing, which further supports the idea that larger γ values lead to overfitting with the target image. Therefore, we select $\gamma = 5$ as a trade-off.

Adversarial Noise Selection Scale ω . As shown in Table 5, the FID (\downarrow) and Intra-LPIPS (\uparrow) scores for FFHQ \rightarrow Sunglasses vary with an increase in the omega (ω) value (from Equation (8)). Initially, the FID score decreases as the generated images gradually grow closer to the target image. When $\omega = 0.02$, the FID reaches its lowest value of 18.13. Beyond this point, the FID score increases because the synthesized images become too similar to the target image, which lowers diversity. The Intra-LPIPS score consistently decreases as ω increases, further supporting that larger ω values lead to overfitting with the target image. We also note that the results are relatively stable when ω is between 0.1 and 0.3. As such, we choose $\omega = 0.02$ as a balance between fidelity and diversity.

Table 5: This shows the change in FID (lower is better) and Intra-LPIPS (higher is better) results for FFHQ \rightarrow Sunglasses as the ω value increases.

ω	FID (\downarrow)	Intra-LPIPS (\uparrow)
0.01	18.42	0.616 \pm 0.020
0.02	18.13	0.613 \pm 0.011
0.03	18.42	0.613 \pm 0.016
0.04	19.11	0.614 \pm 0.013
0.05	19.48	0.623 \pm 0.015

Iteration. As illustrated in Table 6, the FID (\downarrow) and Intra-LPIPS (\uparrow) for FFHQ \rightarrow Sunglasses vary as training iterations increase. Initially, the FID value drops significantly as the generated image gradually resembles the target image, reaching its lowest at 18.13 with 300 training iterations. After this point, the FID score stabilizes after around 400 iterations as the synthesized images closely mirror the target image. The Intra-LPIPS score steadily decreases with an increase in iterations up to 400, further suggesting that a higher number of iterations can lead to overfitting to the target image. Therefore, we select 300 as an optimal number of training iterations, offering a balance between image quality and diversity.

Table 6: This shows the change in FID (lower is better) and Intra-LPIPS (higher is better) results for FFHQ \rightarrow Sunglasses as the number of training iterations increases.

Iteration	FID (\downarrow)	Intra-LPIPS (\uparrow)
0	111.32	0.650 \pm 0.071
50	93.82	0.666 \pm 0.020
100	58.27	0.666 \pm 0.015
150	31.08	0.654 \pm 0.017
200	19.51	0.635 \pm 0.014
250	18.34	0.624 \pm 0.011
300	18.13	0.613 \pm 0.011
350	21.17	0.604 \pm 0.016
400	21.17	0.608 \pm 0.019

B Proofs

B.1 Source and Target Model Distance

This subsection introduces the detailed derivation of source and target model distance, Equation (5) as following:

$$\begin{aligned}
& \text{D}_{\text{KL}}(p_{\theta_{\mathcal{S}},\phi}(x_{t-1}^{\mathcal{S}}|x_t), p_{\theta_{\mathcal{T}},\phi}(x_{t-1}^{\mathcal{T}}|x_t)) \\
&= \text{D}_{\text{KL}}(p_{\theta_{(\mathcal{S},\mathcal{T}),\phi}(x_{t-1}|x_t, y = \mathcal{S})}, p_{\theta_{(\mathcal{S},\mathcal{T}),\phi}(x_{t-1}|x_t, y = \mathcal{T})}) \\
&\approx \text{D}_{\text{KL}}(\mathcal{N}(x_{t-1}; \mu_{\theta_{(\mathcal{S},\mathcal{T})}} + \sigma_t^2 \gamma \nabla_{x_t} \log p_{\phi}(y = \mathcal{S}|x_t), \sigma_t^2 \mathbf{I}), \mathcal{N}(x_{t-1}; \mu_{\theta_{(\mathcal{S},\mathcal{T})}} + \sigma_t^2 \gamma \nabla_{x_t} \log p_{\phi}(y = \mathcal{T}|x_t), \sigma_t^2 \mathbf{I})) \\
&= \mathbb{E}_{t,x_0,\epsilon} \left[\frac{1}{2\sigma_t^2} \left\| \mu_{\theta_{(\mathcal{S},\mathcal{T})}} + \sigma_t^2 \gamma \nabla_{x_t} \log p_{\phi}(y = \mathcal{S}|x_t) - \mu_{\theta_{(\mathcal{S},\mathcal{T})}} - \sigma_t^2 \gamma \nabla_{x_t} \log p_{\phi}(y = \mathcal{T}|x_t) \right\|^2 \right] \\
&= \mathbb{E}_{t,x_0,\epsilon} \left[C_1 \left\| \nabla_{x_t} \log p_{\phi}(y = \mathcal{S}|x_t) - \nabla_{x_t} \log p_{\phi}(y = \mathcal{T}|x_t) \right\|^2 \right], \tag{11}
\end{aligned}$$

where $C_1 = \gamma/2$ is a constant. Since C_1 is scale constant, we can ignore this scale constant for the transfer gap and Equation (11) is the same as Equation (5).

B.2 Similarity-Guided Loss

In this subsection, we introduce the full proof how we get similarity-guided loss, Equation (6). Inspired by [9], training is carried out by optimizing the typical variational limit on negative log-likelihood:

$$\begin{aligned}
\mathbb{E}[-\log p_{\theta,\phi}(x_0|y = \mathcal{T})] &\leq \mathbb{E}_q \left[-\log \frac{p_{\theta,\phi}(x_{0:T}|y = \mathcal{T})}{q(x_{1:T}|x_0)} \right] \\
&= \mathbb{E}_q \left[-\log p(x_T) - \sum_{t \geq 1} \log \frac{p_{\theta,\phi}(x_{t-1}|x_t, y = \mathcal{T})}{q(x_t|x_{t-1})} \right] := L. \tag{12}
\end{aligned}$$

According to [9], $q(x_t|x_0)$ can be expressed as:

$$q(x_t|x_0) = \mathcal{N}(x_t; \sqrt{\bar{\alpha}_t}x_0, (1 - \bar{\alpha}_t)). \tag{13}$$

Training efficiency can be obtained by optimizing random elements of L (12) using stochastic gradient descent. Further progress is made via variance reduction by rewriting L (12) with Equation (13) as Ho et al. [9]:

$$\begin{aligned}
L &= \mathbb{E}_q \left[\underbrace{\text{D}_{\text{KL}}(q(x_T|x_0), p(x_T|y = \mathcal{T}))}_{L_T} + \sum_{t > 1} \underbrace{\text{D}_{\text{KL}}(q(x_{t-1}|x_t, x_0), p_{\theta,\phi}(x_{t-1}|x_t, y = \mathcal{T}))}_{L_{t-1}} \right. \\
&\quad \left. - \underbrace{\log p_{\theta,\phi}(x_0|x_1, y = \mathcal{T})}_{L_0} \right]. \tag{14}
\end{aligned}$$

As Dhariwal and Nichol [5], the conditional reverse noise process $p_{\theta,\phi}(x_{t-1}|x_t, y)$ is:

$$p_{\theta,\phi}(x_{t-1}|x_t, y) \approx \mathcal{N}(x_{t-1}; \mu_{\theta}(x_t, t) + \sigma_t^2 \gamma \nabla_{x_t} \log p_{\phi}(y|x_t), \sigma_t^2 \mathbf{I}). \tag{15}$$

The L_{t-1} with Equation (15) can be rewritten as:

$$\begin{aligned}
L_{t-1} &:= \text{D}_{\text{KL}}(q(x_{t-1}|x_t, x_0), p_{\theta,\phi}(x_{t-1}|x_t, y = \mathcal{T})) \\
&= \mathbb{E}_q \left[\frac{1}{2\sigma_t^2} \left\| \tilde{\mu}_t(x_t, x_0) - \mu_t(x_t, x_0) - \sigma_t^2 \gamma \nabla_{x_t} \log p_{\phi}(y|x_t) \right\|^2 \right] \\
&= \mathbb{E}_{t,x_0,\epsilon} \left[C_2 \left\| \epsilon_t - \epsilon_{\theta}(x_t, t) - \hat{\sigma}_t^2 \gamma \nabla_{x_t} \log p_{\phi}(y = \mathcal{T}|x_t) \right\|^2 \right], \tag{16}
\end{aligned}$$

where $C_2 = \frac{\beta_t^2}{2\sigma_t^2 \alpha_t (1 - \bar{\alpha}_t)}$ is a constant, and $\hat{\sigma}_t = (1 - \bar{\alpha}_{t-1}) \sqrt{\frac{\alpha_t}{1 - \bar{\alpha}_t}}$. We define the L_{t-1} as similarity-guided DPMs train loss and we will ignore the C_2 for better results during training as [9].

C Limitation

In this subsection, we acknowledge some limitations of our method. Given that our goal is to transfer the image from the source domain to the target domain, the images we synthesize will feature

characteristics specific to the target domain, such as sunglasses as shown in Figure 4. This can potentially lead to inconsistency in the generated images and there is a risk of privacy leakage. For instance, the reflection in the sunglasses seen in the 3rd and 4th columns of the 4th row in Figure 4 is very similar to the one in the target image. This could potentially reveal sensitive information from the target domain, which is an issue that needs careful consideration in applying this method.

D Samples

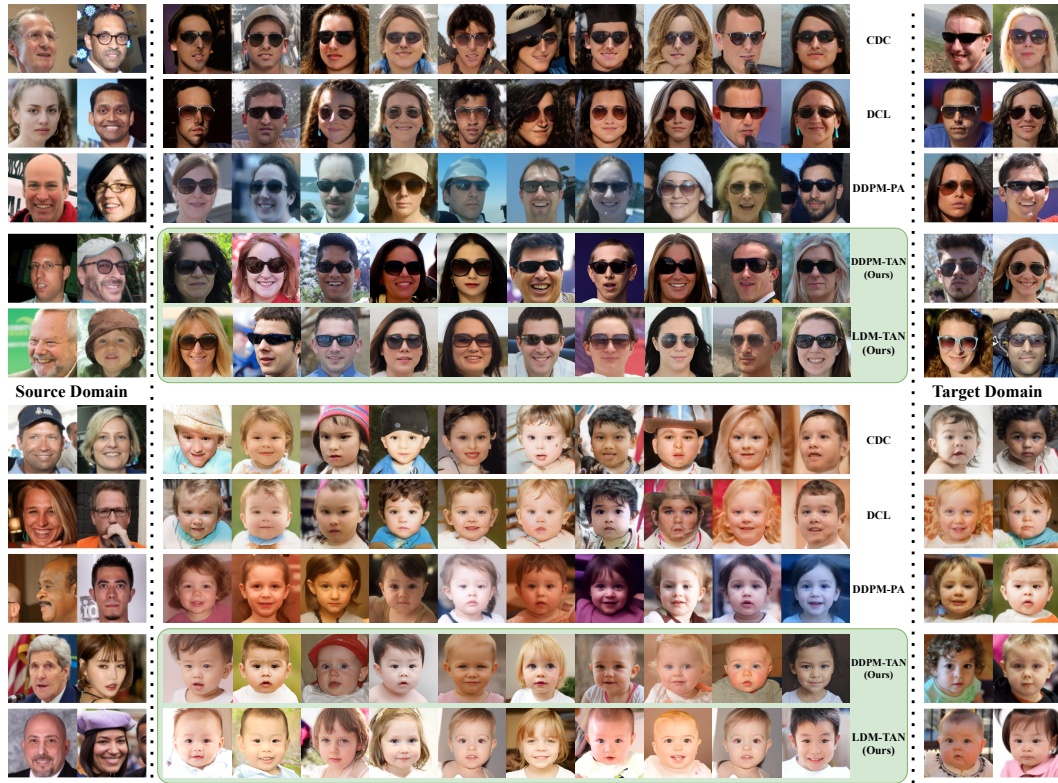


Figure 5: The 10-shot image generation samples on FFHQ \rightarrow Sunglasses and FFHQ \rightarrow Babies.